Research Article

International Journal of
Protective Structures

International Journal of Protective Structures
1–21

DOI: 10.1177/2041419619900517
journals.sagepub.com/home/prs
SAGE

On the effectiveness of ventilation to mitigate the damage of spherical membrane vessels subjected to internal detonations

Francisco Hernandez[1], Xihong Zhang[2] and Hong Hao[2]

Abstract

This article conducts a comparative study on the effectiveness of ventilation to mitigate blasting effects on spherical chambers subjected to internal detonations of high explosives through finite element analysis using the software package AUTODYN. Numerical simulations show that ventilation is ineffective in mitigating the damage of spherical chambers subjected to internal high explosives explosions because the chamber response is mainly described by high-frequency membrane modes. Openings do not reduce the chamber response despite they can reduce the blast overpressure after the chamber reaches its peak response. Worse still, openings lead to stress concentration, which weakens the structure. Therefore, small openings may reduce the capacity of the chamber to resist internal explosions. In addition, because large shock waves impose the chamber to respond to a reverberation frequency associated with the re-reflected shock wave pulses, secondary re-reflected shock waves can govern the chamber response, and plastic/elastic resonance can occur to the chamber. Simulations show that the time lag between the first and the second shock wave ranges from 3 to 7 times the arrival time of the first shock wave, implying that the current simplified design approach should be revised. The response of chambers subjected to eccentric detonations is also studied. Results show that due to asymmetric explosions, other membrane modes may govern the chamber response and causes localized damage, implying that ventilation is also ineffective to mitigate the damage of spherical chambers subjected to eccentric detonations.

Keywords

Confined explosions, AUTODYN, gas pressure component, afterburning, plastic resonance, quasi-static temperature

[1]School of Civil Engineering, University of Chile, Santiago, Chile
[2]Department of Civil Engineering, Curtin University, Bentley, WA, Australia

Corresponding author:
Francisco Hernandez, School of Civil Engineering, University of Chile, Av. Blanco Encalada 2002, Santiago 8370449, Chile.
Email: fhernandezp@ing.uchile.cl

Introduction

Membrane chambers are curved vessels that display low bending stresses in comparison to membrane stresses when they are subjected to internal or external pressures. If the wall thickness of the chamber is smaller than 10 times the mean radius, the membrane stresses become dominant, and bending stresses can be virtually ignored. When the chamber walls offer resistance to bending, flexural bending stresses occur in addition to membrane stresses. For example, flat surfaces or shallow conical heads are susceptible to significant bending stresses that are commonly concentrated around their boundaries. In other words, flexural walls are inefficient geometries because stresses are concentrated in small portions reducing significantly the internal energy that the chamber is able to absorb; in contrast, membrane vessels show an almost uniform stress distribution that involves the response of the entire chamber. Therefore, the preferred shapes that are employed for the construction and design of pressure vessels are spheres, cylinders, cones, ellipsoids, tori, or a combination of these geometries.

The membrane response of a pressure vessel is commonly associated with a high stiffness that results in high natural frequencies. For example, the natural frequency associated with the radial breathing mode (RBM) of steel monobloc spherical chambers, $f_n = \sqrt{E/2 \cdot \pi^2 \cdot \rho(1-\nu) \cdot a^2}$ (Baker and Allen, 1958), ranges, respectively, from 0.5 to 3.0 kHz for $a = 3000$ mm and $a = 500$ mm, where a is the mean chamber radius in millimeter, $\rho = 7800\,\mathrm{kg/m^3}$ is the material density, $\nu = 0.28$ is Poisson's ratio, and $E = 217\,\mathrm{GPa}$ is the material Young's modulus. These high natural frequencies are in the same order of magnitude of the reverberation frequency associated with secondary re-reflected shock waves (SWs), which are generated when an internal detonation of a high explosive (HE) occurs inside a fully confined (FC) blast chamber. Therefore, spherical chambers may experience resonant responses due to multiple re-reflected shock waves (Buzukov, 1980; Hernandez, 2016; Hernandez et al., 2019; Zhdan, 1981).

Simplified analysis using the single-degree-of-freedom (SDOF) method is commonly employed in design practice to analyze the blast response of spherical blast chambers. The SDOF approach assumed perfect spherical symmetry, and the system is subjected to a concentric spherical HE detonation; as a result, the radial response of the chambers is exclusively described by the RBM. It also assumes that the pressure components (first shock wave, re-reflected shock waves, and the gas pressure) can be modeled by a transient uniform radial pressure, which acts synchronically on the entire chamber wall. The solution of the SDOF system considering a perfect elastic–plastic response was analyzed by Hernandez et al. (2019), concluding that all pressure components contribute significantly to the chamber response. The secondary re-reflected shock waves can increase the peak response of spherical chambers up to 85% when elastic or plastic resonance occurs. In fact, chamber resonance was observed when re-reflected secondary shock waves coincide with a positive radial velocity of the camber wall (Hernandez et al., 2019), which increases the work that is done by blast pressure and the internal energy absorbed by the chamber. The gas pressure component can also increase the chamber response, particularly when ductile chambers are analyzed. Previous studies found that the gas pressure component could increase the ductility ratio up to 40% (when the chamber shows a ductility ratio of 5 associated with the first shock wave only; Hernandez et al., 2019). Thus, it is inaccurate to assume that the first shock wave plays a dominant role and ignores the effect of other pressure components such as simplified approaches suggest (Baker and Allen, 1958; Dong et al., 2012). It was also demonstrated by Hernandez et al. (2019) that because the gas pressure is not released quick enough, spherical chambers can rapidly reach the peak response. As a result, the gas pressure cannot be significantly relieved by a relatively small vent on the chamber (10%–20% of the total chamber surface area), implying that small ventilation could

be ineffective in mitigating the damage of spherical chambers. Nevertheless, ventilation can be useful to reduce the quasi-static (QS) high temperature associated with the gas that remains inside the chamber after the dynamic response phase is reached in a FC spherical chamber subjected to an internal HE detonation.

The elastic resonance of spherical chambers subjected to concentric HE detonations was first observed by Zhdan (1981). Zhdan described and solved a one-dimensional (1D) gas-dynamic system of equations to determine the blast load that acts on rigid walls of spherical chambers. It was found that the period of intrinsic oscillation of the pressure can coincide or be a multiple of the natural chamber period; therefore, "the effect of macro-pulsations at the wall has been derived; and the possibility of resonance of the chamber has been established and the corresponding condition noted" (Zhdan, 1981). Similarly, Buzukov (1980) investigated experimentally the responses of cylindrical chambers subjected to the detonation of DSh-A explosive in strips. It was found that the secondary deformation of the chamber is due to resonance arising from the combination of the longitudinal and radial vibration of several harmonics. Results also indicated that the leading cause of the increasing strain lies in the repeatedly reflected shock waves because, under certain conditions, the interval between the pulses loads is close to the period of oscillation of the body. Buzukov (1980) reported that 10 relatively strong reflected shock waves were observed during his experimental study. The author also observed that the arrival time related to the second shock wave and subsequent reflected shock waves were not proportional to the arrival time of the first shock wave. As a consequence, the simplified approach proposed by Anderson et al. (1983) to estimate the effect of the shock wave reflection should be further reviewed when the resonance phenomena need to be accounted for.

Comprehensive numerical modeling has also been conducted to study the blast response of blast chambers. Finite element analysis (FEA) and coupled fluid dynamics (CFD) methods, with coupled or uncoupled Lagrange–Euler algorithms, have been developed by different researchers (Dong et al., 2012; Trabia et al., 2008), which enable accurate modeling of the interactions between gaseous explosive products, that is, air, gases, fluids, and structural elements, which can also be used to model more complex but realistic phenomena such as the presence of nozzles, complex geometries, effects of obstructions, different explosive shapes, diverse explosive materials, changes of ignition points (e.g. eccentricities), strain growth phenomena, multiple initial conditions (e.g. pressure, temperature, medium of propagation), nonlinear structural materials, the effect of three-dimensional (3D) membrane and bending modes, different pressure vessel technologies, and other kinds of singularities that simplified method cannot take into account. FEA can also be used to perform parametric simulations to evaluate the consequences of these variables and to verify different design scenarios. Till now, there is no study yet using a detailed numerical model to investigate the effectiveness of opening for spherical chambers under internal blast loading.

In this study, a 3D model of blast chambers with and without ventilation opening is carried out. The chamber model is coupled with an air blast domain. Comparisons are made between the numerical results from the 3D model and the simplified SDOF model as well as a 1D numerical model. The accuracy of these methods in predicting blast overpressures for both concentric and eccentric detonations is compared. The responses of the spherical chambers predicted using these methods are also evaluated.

Spherical chambers subjected to concentric TNT detonations

Numerical simulations are carried out using the software package ANSYS AUTODYN v14.0. A detailed numerical model of the spherical chamber subjected to concentric trinitrotoluene (TNT) detonation is generated and simulated. As shown in Figure 1, a monobloc spherical chamber with

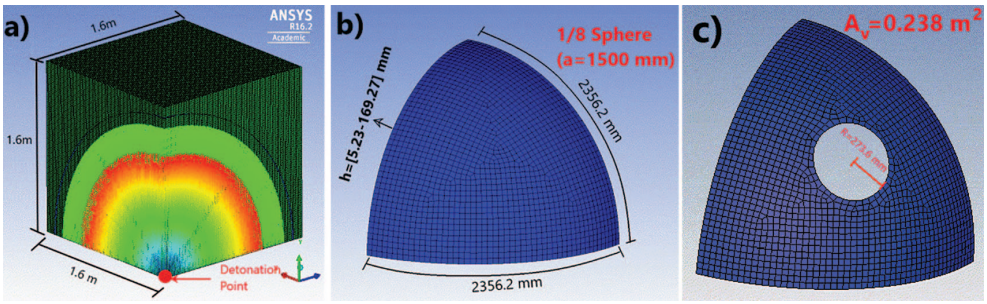

Figure 1. AUTODYN 3D model of fully confined (FC) and partially confined (PC) chambers: (a) Euler mesh and initial remapped shock wave, (b) FC Lagrange shell mesh, and (c) PC Lagrange shell mesh.

a mean radius $a = 1500$ mm is generated. Two wall thicknesses are considered, which are related to two different performance levels: ductility ratios equal to 1.0 and 5.0. The chambers with and without openings are both modeled to evaluate the effect of ventilation. Chambers with opening, that is, partially confined (PC) chambers, are modeled with eight circular openings (273.6 mm radius) that provides an equivalent vent area $A_v / A_{chamber} = 6.72\%$ (where A_v is the total vent area and $A_{chamber}$ is the total surface). The value corresponds to the maximum vent area that can be employed by using Anderson's approach (Anderson et al., 1983) to estimate the gas pressure component for PC chambers subjected to internal TNT detonations; 7, 15, 30, and 120 kg of spherical TNT charges are modeled in this study. Considering symmetry, only one-eighth of the spherical chamber is modeled to save computational time. Fully coupled Euler/Lagrange interaction is employed. Remapping techniques were used, that is, an initial 1D Euler multimaterial simulation with a finer mesh (0.2 mm size) was employed to simulate the initial radial propagation before that the first shock wave reaches the spherical chamber wall. A cubical multimaterial 3D Euler elements of 13.3 mm edge sizes are employed. This implies that a total of 1,728,000 elements are used to model air and TNT, by using a Euler domain size of 1.6 m × 1.6 m × 1.6 m = 4.096 m^3 (different meshing sizes were considered to verify mesh effects, which are later discussed in section "Mesh size effect"). The shell thickness was twice of the Euler element size (i.e. 27 mm) in order to ensure the proper Euler/Lagrange interaction. Five layers of shell elements were used to model the blast chamber (1300 elements).

Material models

The JWL EOS with the AUTODYN's default parameters is employed to model TNT gas products

$$P_{TNT}^{JWL}\left(v, E^{TNT}\right) = A \cdot e^{-R1 \cdot v} \cdot \left[1 - \frac{\omega}{v \cdot R_1}\right] + B \cdot e^{-R_2 \cdot v} \cdot \left[1 - \frac{\omega}{v \cdot R_2}\right] + \frac{\omega \cdot \rho_0^{TNT} \cdot E^{TNT}}{v} \tag{1}$$

where $v = \rho_0^{TNT} / \rho^{TNT}$, $A = 3.7377 \times 10^8$ kPa, $B = 3.7471 \times 10^6$ kPa, $R_1 = 4.15$, $R_2 = 0.9$, and $\omega = 0.35$.

Similarly, the ideal gas EOS is used for air (with $\gamma_{air} = 1.4$)

$$P_{air}^{ideal}\left(\rho_{air}, E_{air}\right) = \rho_{air} \cdot \left(\gamma_{air} - 1\right) \cdot E_{air} \tag{2}$$

Table 1. Parameters used in the simulation (a = 1500 mm).

TNT charge (W)	7 kg	15 kg	30 kg	120 kg
Thickness ($h_{\mu=5}$) μ = 5	5.23 mm	9.62 mm	16.84 mm	54.93 mm
Thickness ($h_{\mu=1}$) μ = 1	15.58 mm	28.84 mm	50.84 mm	169.27 mm
R	100.8 mm	130.0 mm	163.8 mm	260.0 mm
$\bar{r}$	14.85	11.50	9.11	5.66
$\bar{r} \times R/82$	18.26 mm	18.23 mm	18.19 mm	17.96 mm
$\bar{r} \times R / 336$	–	–	4.44 mm	4.38 mm
W/V_{vessel}	0.498 kg/m^3	1.071 kg/m^3	2.158 kg/m^3	8.972 kg/m^3
ΔE_{ad}	4085 kJ/kg	1407 kJ/kg	744.3 kJ/kg	0 kJ/kg
P_{UFC}	1570 kPa	2165 kPa	3544 kPa	11337 kPa
t_a	0.65 ms	0.53 ms	0.44 ms	0.34 ms
$5x\left(t_a + t_r\right)$	3.46 ms	2.92 ms	2.50 ms	2.08 ms

TNT: trinitrotoluene.

The initial internal energy and density are selected, assuming that air is at standard temperature and pressure (*stp*), that is, 298 K and 1 atm. Therefore, $E_0^{air} = 2.068 \times 10^5$ J/kg is the initial specific internal energy of air and $\rho_0^{air} = 0.001225$ g/cm^3 is the initial air density. Similarly, the initial TNT density is $\rho_0^{\text{TNT}} = 1.63$ g/cm^3 and $E_0^{\text{TNT}} = 36.8098 \times 10^6$ J/kg. The same additional afterburning energy is used for FC and PC explosions.

A bilinear isotropic hardening material (perfect elastic–plastic material) for steel chamber with properties is associated with steel BHW35 with density $\rho_s = 7800$ kg / m^3, bulk modulus $K = 1.644 \times 10^8$ kPa, shear modulus $G = 84.76$ GPa, Young's modulus $E = 2.17 \times 10^5$ MPa, and a yielding strength $\sigma_y = 3.9 \times 10^5$ kPa. Strain rate effect, viscous elastic damping, and thermal effects are ignored.

Table 1 summarizes parameters used for simulations, where W is the concentric charge weight (ignited at the center of the chamber and has a spherical shape); h is the thickness of the spherical blast chamber (for ductility ratios μ = 1 and μ = 5 following Case 1S in Hernandez et al., 2019); R is the initial TNT charge radius; $\bar{r} = r / R$ is the relative distance (Shin et al., 2014), where $r = a - h_{..=5} / 2$ is the distance from the TNT charge to the chamber wall); V_{vessel} is the vessel's volume; ΔE_{ad} is the additional afterburning energy; P_{UFC} is the absolute QS gas pressure according to UFC (UFC 3-340-02, 2008); t_a is the arrival time of the first shock wave; and $t_r = i_r \cdot 2 / p_r$ is the duration of the equivalent triangular first shock wave pulse that is obtained from the UFC (UFC 3-340-02, 2008), based on the reflected impulse (i_r) and the reflected pressure (p_r).

Additional afterburning energy and ventilation

The additional afterburning energy (ΔE_{ad}), as listed in Table 1, is selected to ensure the QS gas pressure agrees with the QS gas pressure suggested by the UFC chart (UFC 3-340-02, 2008). It is assumed that the additional afterburning energy starts to be released after the first SW arrives at the chamber wall (t_a , Table 1). It is also assumed that ΔE_{ad} is fully released after the third SW finishes impinging the chamber walls ($5x(t_a + t_r)$, Table 1), which agrees with the gas pressure growing rate observed by Baker from tests of chambers subjected to concentric detonations. It is also worth noting that CFD software packages, such as AUTODYN, are able to model the fluid dynamic process associated with the discharge of gases that occurs throughout openings. For example, Edri et al. (2012) used AUTODYN to model the venting process throughout a small circular opening on

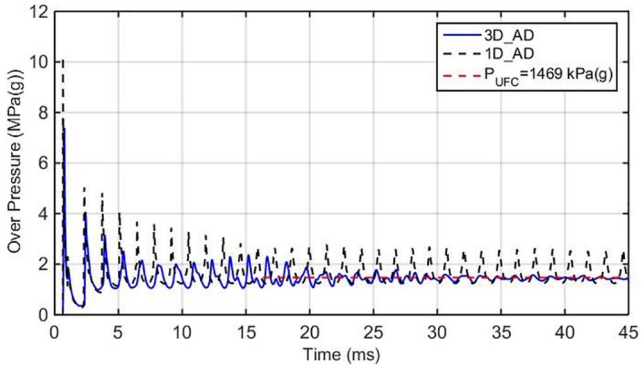

Figure 2. Overpressure time-history obtained with the 3D and 1D models ($a = 1500$ mm, $W = 7$ kg).

a cubical chamber. The pressure time-history obtained using AUTODYN was in good agreement with experimental data.

Mesh size effect

Shin et al. (2014) performed a mesh size sensitivity study to establish the optimum mesh size for 1D analysis using AUTODYN. It was concluded that converged solutions could be achieved for mesh sizes smaller than $r/336$ if $\bar{r} < 4.5$ (near field) or $r/82$ when $\bar{r} > 11$ (far-field). If the same level of convergence for 3D analyses is assumed, it is reasonable to assume that a mesh size of 13.3 mm is suitable for $W = 7$, 15, and 30 kg TNT explosion cases, but it may be not enough for $W = 120$ kg (where 4.4 mm mesh size is required, implying 48 millions of Euler elements). In this study, another 1D model with mesh sizes of 0.75 mm (chamber assumed to be perfectly rigid), together with the 3D model mentioned above, was generated for the FC spherical chamber subjected to a concentric TNT detonation ($W = 7$ kg). Both models use the same additional afterburning energy detailed in Table 1. Figure 2 compares the overpressure results from the two numerical models with those from UFC prediction. It can be found that the 1D model showed a more significant energy error during its numerical solution (equal to 15%).

Figure 3(a) compares the pressure time-histories during the first 20 ms obtained from 1D and 3D analyses (1D_AD and 3D_AD, respectively) as well as the prediction using the a simplified overpressure function that includes three re-reflected shock waves (3S) and the Quasi-Static Gas pressure component (QSG) (Hernandez, 2016). Very similar reflected pressures associated with the first SW (p_r) can be found for the prediction of the simplified overpressure function (10.19 MPa, obtained from the UFC chart) and the 1D analysis (10.21 MPa); about 27.6% smaller reflected pressure ($p_r = 7.38\text{MPa}$) is found on the 3D analysis. A small second shock wave is observed behind the shock front owing to the expansion of HE products (a reverberating shock wave; Buzukov, 1980; Zhdan, 1981), which is not considered by the simplified SDOF approach. Also, the 3D model shows more than 10 significant shock waves, and the 1D analysis shows 33 significant shock waves during the first 45 ms (after ignition) with limited attenuation. The difference is because the 3D model takes into account the fluid/structure interaction, the energy absorbed by the chamber, the imperfect asymmetrical behavior, and energy errors observed during the solution of the 1D FEA.

Table 2 shows the peak reflected pressures, arrival times, and reflected impulses associated with the first 10 shock waves obtained from the 1D analysis, the 3D analysis, and the simplified overpressure function (3S + QSG). It can be observed that the peak reflected pressures predicted by the

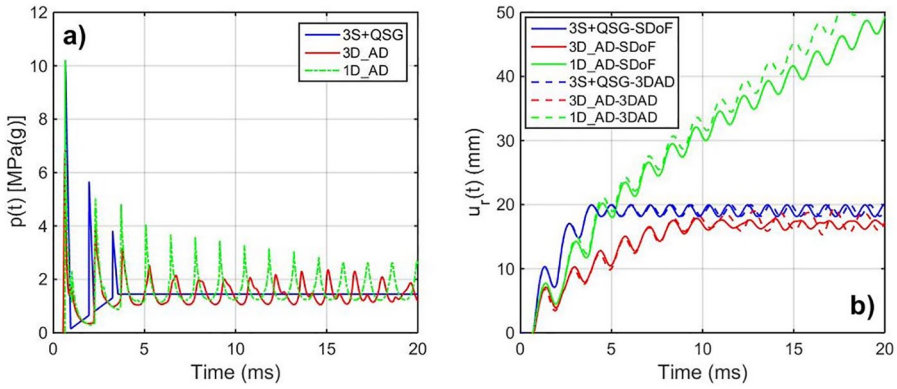

Figure 3. (a) Overpressure time-history from SDOF model, 3D model, and 1D model. (b) Radial response calculated with the equivalent SDOF system assuming coupled or uncoupled 3D analysis.

Table 2. Peak reflected pressure (p_r), arrival times (t_a), and impulses (i_r) related to the first 10 shock waves (SW) for 1D and 3D simulations and the simplified approach.

SW No.	1D model (1D_AD)			3D model (3D_AD)			Simplified SDOF (case 3S + QSG)		
	p_r (MPa)	t_a (ms)	i_r (MPa ms)	p_r (MPa)	t_a (ms)	i_r (MPa ms)	p_r (MPa)	t_a (ms)	i_r (MPa ms)
1	10.21	0.64	2.04	7.58	0.64	2.01	10.19	0.65	1.92
2	2.31	1.01	–	1.69	0.97	–	–	–	–
3	5.02	2.31	2.26	4.05	2.30	1.84	5.67	1.95	2.00
4	4.82	3.71	2.22	3.16	3.81	2.07	3.82	3.25	2.22
5	4.07	5.07	1.74	2.52	5.26	1.93	–	(5.26)	2.08
6	3.68	6.44	2.17	2.15	6.72	2.11	–	(6.72)	2.11
7	3.58	7.78	2.07	1.84	7.99	2.13	–	(7.99)	2.15
8	3.44	9.13	2.18	2.00	9.39	2.06	–	(9.39)	2.06
9	3.27	10.49	2.13	2.06	10.80	2.06	–	(10.8)	2.06
10	3.15	11.84	2.22	2.17	12.21	2.12	–	(12.2)	2.13
	$\frac{1}{t_a} = 714.6\,Hz$		$\sum = 19.03$	$\frac{1}{t_a} = 691.6\,Hz$		$\sum = 18.34$	$\frac{1}{t_a} = 769.2\,Hz$		$\sum = 18.74$

SDOF: single degree of freedom.
t_a is the average time difference between arrival times of subsequent shock waves.

3D model are 35% lower than that from the 1D analysis. The arrival times obtained from the 1D and 3D analyses are slightly different during the initial part of the curve, but the cumulative difference becomes significant after the fourth pulse. And the arrival times associated with the secondary re-reflected pulses calculated with the simplified approach are smaller than those obtained from numerical simulations. Overall, the 1D model shows slightly shorter arrival times than the 3D model. The reflected impulses (obtained between each pressure local minimum) do not show a significant difference between the three models. Nevertheless, similar QS gas pressures are predicted by both the 1D and 3D models, which also agree well with the UFC prediction (1469 kPa), indicating the afterburning energy value was appropriate.

Plastic resonance

Part of the energy, which is allocated in enclosed gases, is absorbed by the chamber due to blast wave/structure interaction. The work that is done by the blast pressure ($W_{gas}(t) = \int p(t) \cdot \dot{u}_r(t) \partial t$, where $\dot{u}_r$ is the chamber radial velocity) is highly related to the internal energy that the chamber absorbs as a result of elastic or plastic deformation. This process is not accounted for the 1D analyses since the chamber was assumed to be rigid ($u_r = 0$). Therefore, uncoupled analyses cannot describe the attenuation of shock waves accurately. However, the 1D uncoupled analyses could be conservative for the design of blast chambers, because it does not take into account the attenuation of shock waves due to the energy absorption of the chamber.

Figure 3(b) shows the radial response of the chamber ($u_r(t)$) calculated by using the pressure time-histories (Figure 3(a)). The radial response of the chamber is obtained using two procedures, that is, the equivalent perfect elastic–plastic SDOF model (Hernandez, 2016) and 3D FEA performed in the software package AUTODYN (3D_AD). The SDOF solution is obtained by considering a perfect elastic–plastic response solved by using Newmark's constant acceleration method (Chopra, 1995). Overall, the equation of motion that describes the radial response ($u_r(t)$) of a spherical chamber subjected to a uniform pressure time-history ($p(t)$) was described by Baker and Allen (1958) as follows

$$\frac{\partial^2 u_r}{\partial t^2} + \omega_n{}^2 \cdot u_r = \frac{p(t)}{\rho \cdot h} \tag{3}$$

where ρ is the material density ($\mathrm{kg/m^3}$), $\omega_n = \sqrt{2 \cdot E / (\rho \cdot (1-\nu) \cdot a^2)}$ is the natural angular frequency, $P_y = 2 \cdot h \cdot \sigma_y / a$ is the yielding pressure, h is the chamber wall thickness (m), E is Young's modulus (Pa), σ_y is the yielding strength (Pa), ν is Poisson's ratio, and a is the mean radius of the spherical chamber (m).

The radial responses 3S + QSG-3DAD and 1D_AD-3DAD are obtained from uncoupled analyses, that is, the pressure time-histories are uniformly applied to the chamber, while the radial response 3D_AD-3DAD refers to a coupled analysis where the Euler/Lagrange interaction was directly accounted. From Figure 3(b), it can be found that the spherical chamber is highly susceptible to plastic resonance. In particular, the pressure time-history associated with the 1D analysis (1D-AD) generates several re-reflected pulses, which frequently coincide with positive radial velocities and triggers amplification at short and long terms. The second SW associated with the pressure profile 3S + QSG coincides with higher radial velocities, causing a significant amplification on the response of the chamber. The smallest amplification caused by the second SW is observed for the pressure time-history 3D-AD. Because this SW coincides with smaller radial velocities, the pulses do not precisely resonant with the RBM. The occurrence of resonance depends on the arrival times associated with the re-reflected SW pulses. Therefore, a small difference in the arrival time can imply a significant difference in the amplification caused by pulses. In general, the arrival times of secondary SWs involve a certain degree of uncertainty. As previously mentioned, the way that the afterburning energy is released can change the arrival time, and the peak reflected pressure associated with each SWs (Hernandez et al., 2016).

The peak RBM response is described by the work that is done by the blast pressure, that is, $u_r^{\max} = f(W_{gas})$. It can be observed that the pressure time-histories, which were obtained with the 1D model (1D_AD), the 3D model (3D_AD), and the SDOF model (3S + QSG), have similar reflected impulse values (i_r) associated with each shock wave (Table 2). However, significant differences in the chamber responses are observed (Figure 3(b)) because shock waves arrive at slightly

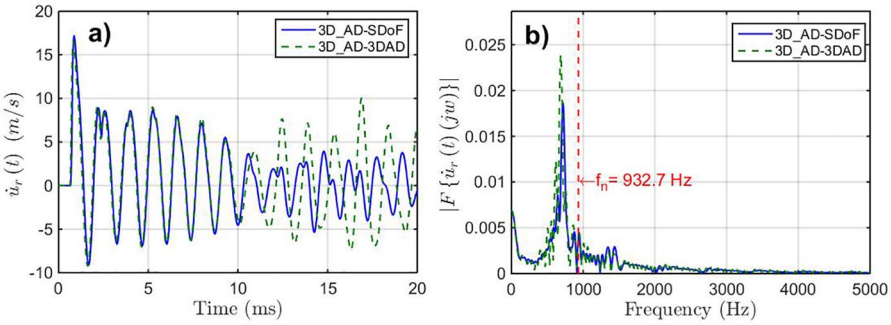

Figure 4. (a) Radial velocity of the chamber and (b) frequency spectrum obtained with the SDOF model and the coupled 3D model.

different times, and the shape of the SWs is not precisely the same (Figure 3(a)). It can also be found that the reflected impulses (i_r) associated with secondary SWs (SW > 3; shown in Table 2) are mainly associated with the gas pressure component, rather than the effect of re-reflected pulses. Therefore, the reflected impulses of Table 2 are not related to the resonant phenomenon. Based on the analysis of the work by blast pressure, it can be concluded that the work of blast pressure increases when the chamber velocity is positive, and it decreases when a negative radial velocity occurs, owing to the fact that overpressure is always positive for confined explosions.

The second effect generated by the gas pressure component refers to the QS stress. The gas pressure component causes uniform tensile membrane stress, which can be obtained from the static part of the equation of motion and equal to $\sigma^{gas}(t) = a \cdot p^{gas}(t) / (2 \cdot h)$ (normal stresses) for spherical chambers, owing to the high natural frequency of the RBM. The membrane stress is a constant, $\sigma^{QS} = a \cdot P_{QS} / (2 \cdot h)$, when the QS pressure (P_{QS}) is reached. Thus, the QS gas pressure increases the average stress of the chamber wall, increasing the chance of the chamber plastic deformation. Since $\sigma^{gas}(t)$ is a QS function, it can be included in the analysis as a yielding strength reduction, that is, $\sigma_y^{eff}(t) = \sigma_y - \sigma^{gas}(t)$. Therefore, the simplified plastic resonance approach suggested by Hernandez et al. (2019) can be improved by considering the equivalent yield strength.

Figure 4 shows that the plastic response of the chamber is mainly governed by the SWs frequency (714.6 and 691.6 Hz; Table 2). This implies that the blast load enforces the structure to respond at the excitation frequency, which is lower than the natural frequency of the chamber (932.7 Hz) when plastic behavior is observed. It can be found that the response obtained from the SDOF analysis is similar to the curve simulated from the 3D model. Therefore, the chamber response is mainly described by the RBM. This can be further proved by the 3D analysis results that show an almost uniform plastic strain distribution and a uniform radial deformation during the simulation (as shown in Figure 10).

From Figure 4(a), it can be observed that during the initial 10 ms, the radial velocity from the SDOF model and the 3D model match closely. When the ninth SW arrives at 10.8 ms (Figure 3 and Table 2), the pulse coincides with a peak radial velocity, which generates an amplification for the 3D analysis. However, this SW does not exactly resonate with the SDOF solution because of a minor time lag between the 3D model and the SDOF analysis. A significant difference can be observed in the radial velocity between the 3D model and the SDOF model indicating that a small uncertainty in the response phase could lead to significant differences in the prediction of the response because the chamber resonance is highly susceptible to small changes in the arrival time of re-reflected shock waves.

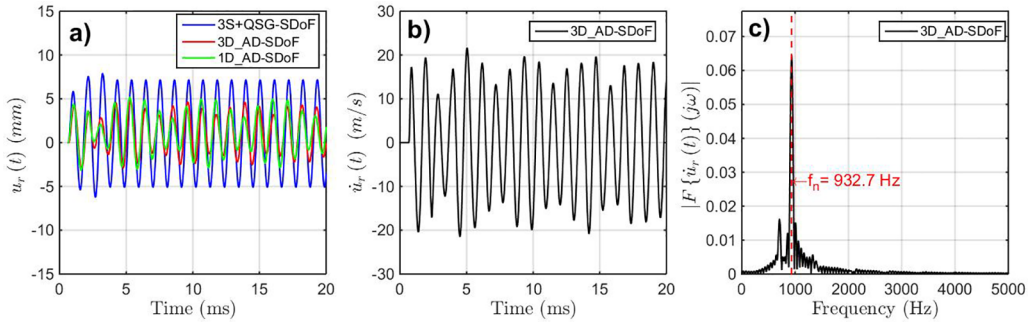

Figure 5. (a) Radial response of the chamber, (b) radial velocity, and (c) frequency spectrum obtained with the SDOF model for the elastic chamber (a = 1500 mm, W = 7 kg).

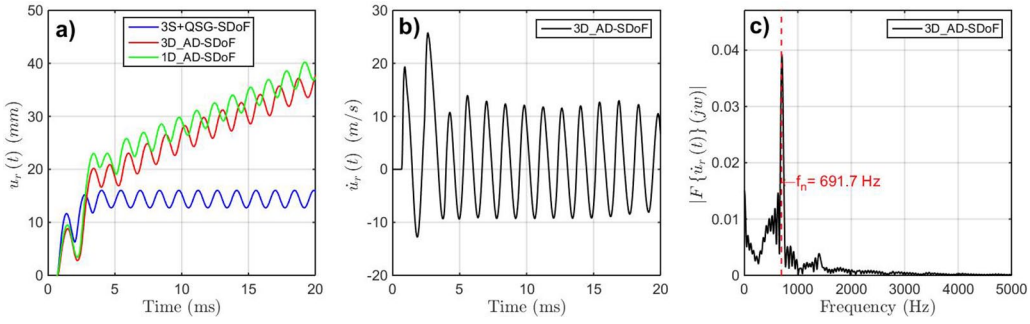

Figure 6. (a) Radial response of the chamber, (b) radial velocity, and (c) frequency spectrum obtained with the SDOF model when $E = 1.1935 \times 10^5$ MPa .

However, the chamber responses are governed by the RBM frequency (932.7 Hz) when it behaves elastically. The chamber response is primarily governed by an impulsive component in agreement with the natural frequency of the system. Figure 5 shows the elastic radial response (displacement and velocity) when an elastic chamber is used for the SDOF analysis (i.e. large σ_y). As can be found, the frequency spectrum is governed by the elastic frequency of the chamber (932.7 Hz), and a secondary peak is related to the frequency related to SWs (691.7 Hz). It can also be observed from Figure 5 that the chamber response is very similar when 1D_AD or 3D_AD pressure time-histories (Figure 3) are used. Resonance is not observed if the SW frequency does not coincide with the natural frequency of the chamber. A beating effect can be observed related to the presence of the natural RBM frequency and the re-reflected SWs frequency on the chamber response but no amplification due to resonance, as observed in Figure 3(b).

Similarly, Figure 6 shows the chamber response and its frequency spectrum when the structure is modified with a natural frequency equal to the re-reflected pulses (i.e. 691.7 Hz). It should be noted that without losing generality, this is artificially achieved by modifying Young's elasticity modulus of steel to $E = 119.35$ GPa . As shown, the obtained chamber response by using the 3D_AD and the 1D_AD pressure time-histories are quite similar. That is, both models show a significant amplification effect due to the re-reflected shock waves for short and long terms. In other words, if the chamber frequency is similar to the frequency of the pulses, small differences in shock wave amplitudes have little influence on the chamber response.

Based on these results, it can be concluded that strong SWs induce force vibration of the chamber and tend to lead to the plastic resonance of the chamber, that is, peaks of SW pulses tend to coincide with peak radial velocities. If blast waves are attenuated, the response of the chamber tends to be governed by its natural frequency; therefore, resonance occurs if the chamber's frequency is near to (or a multiple of) the frequency of SW pulses only.

From Figure 4, it can also be observed that the peak chamber velocity tends to coincide with the re-reflected shock wave peaks when pulses display a significant amplitude. Instead, the peaks in the pressure time-histories do not coincide with radial peak velocities when pulses are not strong enough. In other words, weak pulses are slowly uncoupled to the chamber response, which prevents amplifications. As we can observe in Figure 3, the plastic resonance for the 3D_AD pressure is observed until 10 ms, after which SW pulses and the chamber response are slowly uncoupled, which leads to no plastic amplification. The SDOF system is accurate to simulate the response of spherical chambers subjected to concentric TNT detonations. This is because other asymmetrical and non-asymmetrical modes, related to membrane and bending modes, have an insignificant contribution to the chamber response. Therefore, the blast loading generates a uniform pressure that excites only the RBM. The assumption that the initial three shock waves are the most important and the subsequent SWs can be ignored may not necessarily be accurate for FC spherical chambers, because subsequent re-reflected pulses can cause significant strain growth due to a resonant response. The arrival times that are assumed by the simplified pressure time-history (Case 3S + QSG; Hernandez et al., 2019) associated with secondary re-reflected SWs are smaller than those predicted by the numerical models. Therefore, the simplified approach that considers only the initial three SWs needs to be reviewed as soon as the plastic resonance is highly susceptible to the effect of other secondary SWs.

Venting effects

Ventilation in the chamber could have the following influence on the recorded pressure time-history: (1) reduces the gas pressure component, (2) reduces secondary re-reflected SWs, and (3) the pressure profile is not uniform anymore. In the meanwhile, the first SW is almost unaltered by small openings.

Figure 7 shows the overpressure time-history obtained from coupled 3D model (3D_AD), for the FC case and the PC case when the chamber is subjected to concentric detonations of TNT charges (W = 7, 15, 30, and 120 kg). The pressure time-histories from the 3D model are compared with those estimated using the approaches suggested in the UFC (Case 3S + QSG* and 3S + TG*) by considering three SWs. It is worth noting that the arrival time of the second SW in the UFC model is modified to coincide with the arrival time obtained from the 3D model for the FC case (3D_AD-FC). The third SW is assumed to propagate at the same average speed observed for the second SW. In addition, it has included the gas pressure component that was obtained for the PC case by using the Anderson et al. (1983) approach.

From Figure 7, it is observed that the QS gas pressure that was obtained for the FC case and the 3D model matches closely with that given by UFC (Table 1) if an appropriate additional afterburning energy value is used (Hernandez et al., 2016). Similarly, the gas pressure for the PC condition agrees well with the pressure component that is suggested by Anderson et al. (1983), which was obtained from adjustment of experimental data, and it is reasonably similar to the simplified triangular gas pressure component suggested by the UFC (which was also obtained from experimental data, but based on a simplified triangular curve). In other words, the pressure gas component obtained from the numerical solution is validated because it matches the experimental curves for the fully and PC cases. Therefore, it can be concluded that ventilation is correctly modeled when

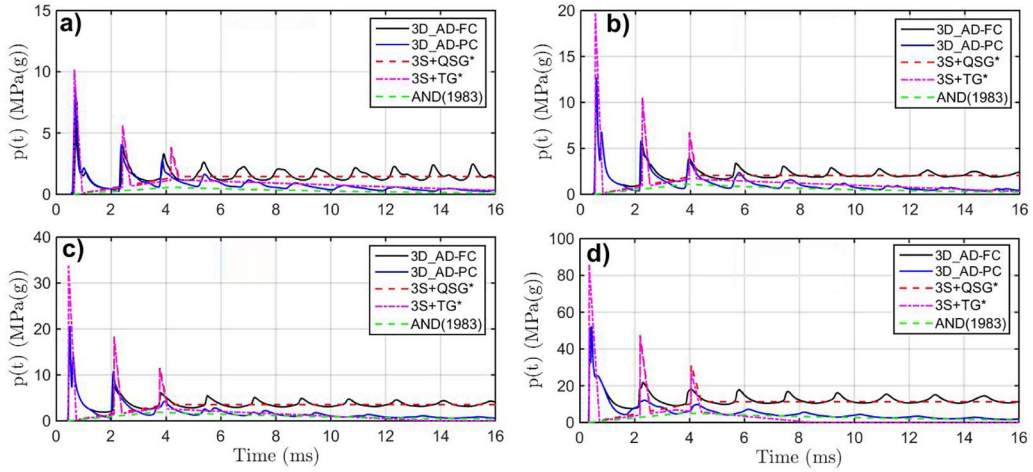

Figure 7. Overpressure time-history obtained for the fully confined (FC) and partially confined (PC) cases using the 3D model and the simplified SDOF model: (a) $W = 7$ kg, (b) $W = 15$ kg, (c) $W = 30$ kg, and (d) $W = 120$ kg.

Table 3. The first SW and the second SW arrival time and the peak reflected pressure.

W (kg)	p_r (MPa)	p_r^{UFC} (MPa)	ε_r (%)	i_r (1st SW) (MPa ms)	i_r^{MSP} (MPa ms)	εr (%)	$t\,t_a^{(2SW)}$ (ms)	$3ta$ (ms)	$\frac{t_a^{(2SW)}}{t_a}$
7	7.58	10.19	−25.6	2.01	1.92	4.7	2.413	1.947	3.72
15	12.65	19.70	−35.8	3.96	3.57	11.1	2.247	1.578	4.27
30	20.57	33.79	−39.1	7.05	6.38	10.4	2.106	1.317	4.80
120	52.05	85.79	−39.3	28.55	20.52	39.1	2.196	0.992	6.64

openings are incorporated in AUTODYN. In addition, it can be concluded that the gas pressure component is not affected by the selected mesh size (13.3 mm).

From Figure 7, it can be found that a smaller peak reflected pressure for the first SW is predicted by the 3D model, which is caused because of the influence of mesh size (as it was discussed in section "Mesh size effect"). The selected mesh might slightly underestimate the peaks of the reflected shock waves, but it generates similar reflected impulses (Table 2). Therefore, the peak values of the re-reflected SWs could be reduced when a relatively coarse mesh is used that might affect slightly the conclusion about the effectiveness of ventilation associated with mitigation of re-reflected shock waves. The effect of the gas pressure component becomes relatively more important when a coarse mesh is employed, which is conservative for the evaluation of the effectiveness of ventilation to mitigate damage related to the reduction of the gas pressure component.

Several re-reflected SWs with large amplitudes can be observed on the 3D model, which could cause amplification of chamber response due to resonance. For the PC condition, SWs decay faster than the FC condition.

Table 3 shows the comparison between the peaks reflected pressure and the reflected impulses (including the gas pressure effect) related to the first SW for the FC case. In general, the reflected peak pressures (p_r) from the 3D model are smaller than those predicted from the UFC approach. It indicates that the mesh size effect causes the peak reflected pressure to be underestimated by

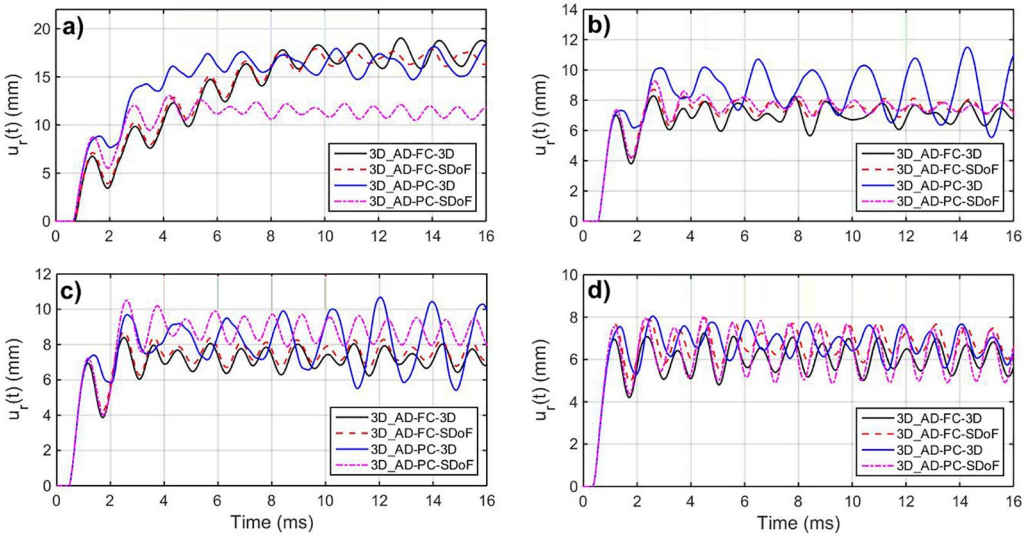

Figure 8. Radial displacement response associated with the pressure time-history obtained for the fully confined (3D_AD-FC) and partially confined (3D_AD-PC) cases according to the 3D model and the SDOF model: (a) $W = 7$ kg, $h = 5.23$ mm; (b) $W = 15$ kg, $h = 9.62$ mm; (c) $W = 30$ kg, $h = 16.84$; and (d) $W = 120$ kg, $h = 54.93$.

25.6%–39.3%. In contrast, the reflected impulse related to the first SW from the 3D model is higher than that from the simplified UFC model. This is because a secondary reverberating shock wave is modeled by the 3D model. The arrival time related to the second SW ($t_a^{(2SW)}$) is significantly longer than the value that is traditionally assumed by using the simplified approach ($3t_a$), which indicates that the second SW propagates slower than the first SW, showing that the second SW arrives between $\left[3 \cdot t_a - 7 \cdot t_a\right]$.

Figure 8 compares the radial displacement from the coupled 3D model and the uncoupled equivalent SDOF system using the pressure time-histories obtained for the FC case (3D_AD-FC) and the PC case (3D_AD-PC; Figure 7). These results are calculated by using the chamber thickness associated with a ductility ratio of 5 for Case 1S ($h_{\mu=5}$ of Table 1). It can be observed that the radial displacement obtained for the FC case (3D_AD-FC-3D) is practically the same at any point in the chamber. In contrast, the radial displacement that was obtained for PC chambers (3D_AD-PC-3D) refers to points far from the opening (indicated as points 1, 2, and 3 in Figure 9). These points show significant differences with other points of the chamber (which are closer to the opening). From Figure 8, it can be observed that the FC response of the chamber is governed by the RBM (SDOF system). This is because there are minor differences between the 3D model (3D_AD-FC-3D) and the SDOF (3D_AD-FC-SDOF), which is due to a slight time lag between responses, which can be attributed to numerical errors and small numerical differences between the 3D model and the simplified SDOF model.

Radial displacements obtained for the PC case (at points far from openings) are in the same order of magnitude with those obtained from the FC case, which indicates that ventilation is not sufficient to reduce structural responses. The chamber response associated with the PC cases obtained from the 3D model and the equivalent SDOF approach shows significant differences. This is because the 3D modeled chamber response is described by several modes rather than only the RBM. This can be proved by the response of case 3D_AD-PC-3D, which is governed by lower frequencies than the

Table 4. Ductility ratio after first SW (1), second SW (2), and final (f).

Case No.	$W=7$ kg			$W=15$ kg			$W=30$ kg			$W=120$ kg		
	$\mu^{(1)}$	$\mu^{(2)}$	$\mu^{(f)}$	$\mu^{(1)}$	$\mu^{(2)}$	$\mu^{(f)}$	$\mu^{(1)}$	$\mu^{(2)}$	$\mu^{(f)}$	$\mu^{(1)}$	$\mu^{(2)}$	$\mu^{(f)}$
3D_AD-FC-3D	3.5	5.1	9.8	3.6	4.3	4.3	3.6	4.3	4.3	3.6	3.6	3.7
3D_AD-FC-SDOF	3.7	5.3	9.2	3.8	4.5	4.5	3.7	4.5	4.5	3.9	4.1	4.1
3D_AD-FC-ε_p	3.5	5.1	9.4	3.7	4.3	4.3	3.6	4.3	4.3	3.6	3.7	3.8
3D_AD_PC_ε_p^{max}	3.5	5.1	9.4	3.7	4.3	4.3	3.6	4.3	4.3	3.6	3.7	3.8
3D_AD-PC-3D	4.5	7.3	9.5	3.8	5.2	5.9	3.8	5.0	5.5	3.9	4.1	4.1
3D_AD-PC-SDOF	4.5	6.2	6.7	3.8	4.8	4.8	3.7	5.4	5.4	3.9	4.1	4.1
3D_AD-PC-ε_p	3.3	5.1	6.1	2.8	3.4	3.4	2.7	3.2	3.2	2.4	2.4	2.4
3D_AD_PC_ε_p^{max}	3.3	5.2	6.4	2.9	3.5	3.5	2.8	3.3	3.3	2.4	2.4	2.4

RBM frequency, indicating that other membranes and composite modes are involved in the dynamic response. Results indicate that several re-reflected SWs are strong enough to amplify the radial response when TNT weight $W=7$ kg. This result is consistent with the resonance condition that was established in Hernandez et al. (2019). That is, $\Theta = 2 \cdot t_a / T_n + t_0 / 3 \cdot T_n - t_{max} / T_n + 1/4 \approx 1$ when $W=7$ kg and $h = h_{\mu=5} = 5.23$ mm, indicating that SWs tend to coincide with positive radial velocities. For $W=15$ kg and $W=30$ kg, $\Theta \approx 0.77$ and $\Theta \approx 0.69$, only the first and second SWs are strong enough to amplify the chamber response. For the case that $W=120$ kg, the chamber response was only governed by the first SW because $\Theta \approx 0.40$, which means that secondary re-reflected shock waves coincide with negative velocities and do not resonate. It can also be observed that the PC chambers show higher radial displacements when the response is governed by the first and the second SWs (i.e. $W=15$, 30, and 120 kg in Figure 8). In particular, openings cause that the second SW generates slightly longer radial amplifications than the observed for the FC case. However, the SDOF radial response is mitigated by ventilation when several re-reflected SWs are dominant because ventilation is effective in mitigating long-term SWs ($W=7$ kg in Figure 8). This implies that ventilation might mitigate structure response to some instances when resonance due to multiple shock waves occurs.

Table 4 shows ductility ratios that are obtained as $\mu = u_r^{\max} / u_{ry}$ (where $u_r^{\max}$ is the maximum accumulated radial displacement displayed in Figure 8 and $u_{ry} = \sigma_y \cdot (1-\nu) / (a \cdot E) = 1.941$ mm the RBM yielding displacement). For comparison, Table 4 also shows ductility ratios that are obtained from the effective plastic strain of the 3D model, associated with points that are far from openings (Figure 9), that is, $\mu = \varepsilon_p / (\sqrt{2} \cdot \varepsilon_y) + 1$ (where ε_p is the effective plastic strain computed by the model and $\varepsilon_y = \sigma_y / E = 0.0018$ is the yielding strain). Table 4 summarizes ductility ratios after the first SW, the second SW, and the final computed value (i.e. $t=16$ ms). It also shows the ductility ratios that are calculated from the maximum plastic strain ($\varepsilon_p^{\max}$) associated with top/bottom layers of the shell, which includes the effect of bending strains at these positions. It can be found that a good agreement is obtained for FC chambers in terms of the ductility ratio obtained from all derivations, demonstrating that the chamber response is mainly governed by the RBM. In contrast, the PC chamber shows that other membrane modes contribute significantly to the chamber response because results obtained from the 3D model and the SDOF model are significantly different. Similarly, the ductility ratios that are calculated from the plastic strain (3D_AD-PC-ε_p and 3D_AD_PC_$\varepsilon_p^{\max}$) are considerably smaller than values computed from the displacement response obtained from the 3D model or the SDOF approach, which means that the local radial response disagrees with local strain, implying that damage is not uniformly distributed. It can be observed that there are no significant differences of ductility ratios calculated from the effective

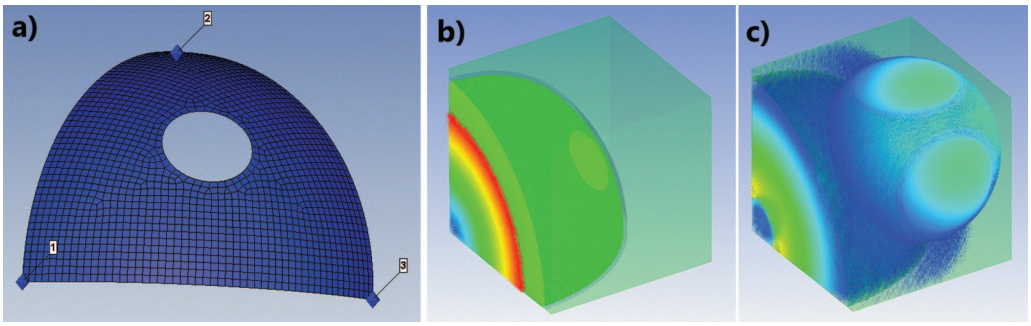

Figure 9. Gauge points far away from openings (related to Figure 8) and gas relief sketch for partially confined chambers: (a) mesh and gauges points, (b) initial remapping velocities associated with the first SW, and (c) relief of gases through openings.

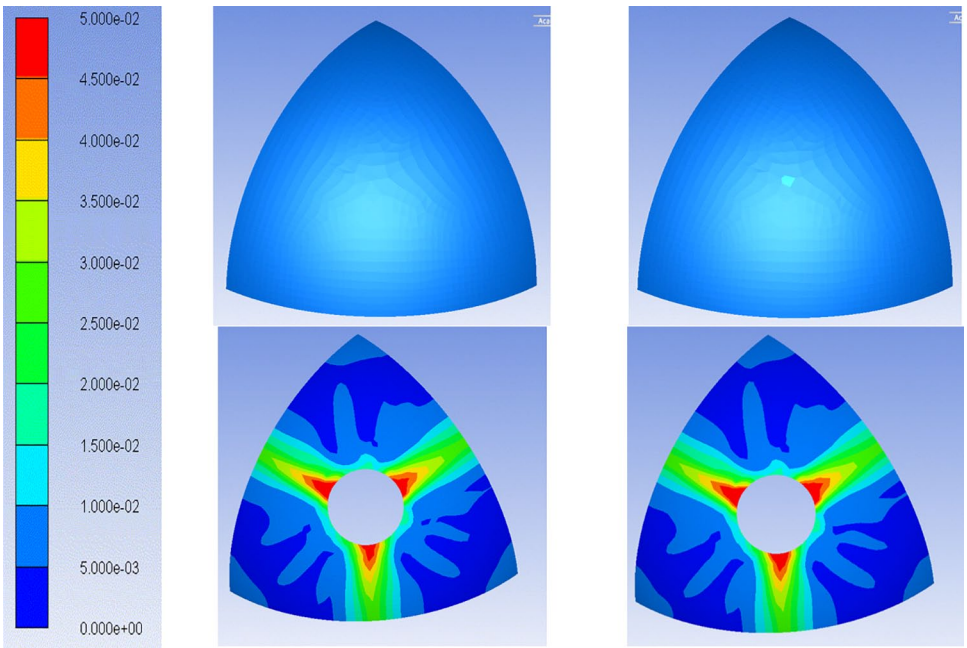

Figure 10. Effective plastic strain (ε_p) related to FC (top) and PC (bottom) chambers ($a = 1500$ mm, $h = 9.62$ mm, and $W = 15$ kg) for the middle-plane (membrane strain, on the left) and surface layer (membrane and bending, on the right).

plastic strain obtained at the mid-plane layer (membrane effect) 3D_AD-PC-ε_p and the plastic strain obtained at the top/bottom layer ($3D\_AD\_PC\_\varepsilon_p^{\max}$), indicating that bending stresses are low, and membrane strains govern the response for points that are far from the openings.

Figure 10 shows the effective plastic strain for the FC and PC chambers. These are the final effective plastic strain at the middle-plane layer associated with the membrane behavior and at the outer/inner surface layer caused by the combined membrane and bending stresses. These results indicate that both the FC and PC chambers are governed by membrane strain. The FC chambers subjected to concentric spherical TNT detonations have an almost uniform plastic strain

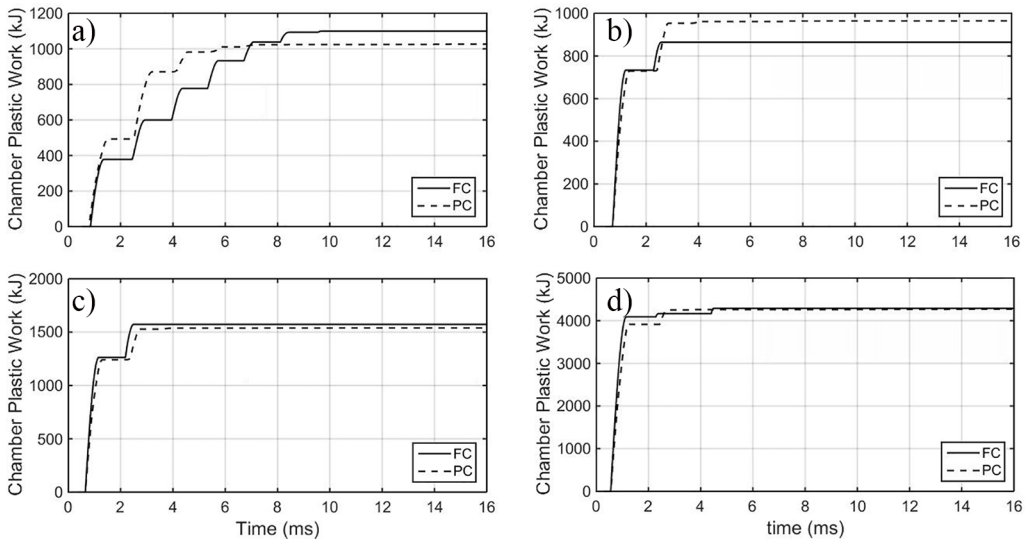

Figure 11. Plastic work for fully confined (FC) and partially confined (PC) chambers: (a) $W = 7$ kg, $h = 5.23$ mm; (b) $W = 15$ kg, $h = 9.62$ mm; (c) $W = 30$ kg, $h = 16.84$ mm; and (d) $W = 120$ kg, $h = 54.93$ mm.

distribution, which confirms that the chamber response is described by the RBM. In contrast, the chambers with openings present a variable distribution of its final effective plastic strain, which is concentrated around the opening and along lines that connect these openings. The effective plastic strain that is observed near to the openings is considerably higher than that observed for zones far-off openings and substantially higher than the values obtained for FC chambers. It can be concluded that openings cause significant geometrical imperfections that trigger the participation of several membrane modes on the chamber response. This asymmetrical membrane response generates stress concentration around openings that produce severe local damage. In contrast, points far-off the opening show slightly lower local damage than FC chambers.

Figure 11 shows the plastic work that is calculated using the 3D model. It can be observed that at the end of the simulation, there are no significant differences between the PC and FC chambers, which means the energy absorbed by the chamber (both the global chamber response and damage) does not change significantly for either chamber. Although the overpressure time-history for the PC case is mitigated by ventilation, opening leads to weak zones that experience more significant plastic deformations and absorb extra energy. Therefore, chambers with or without openings absorb similar plastic energy. But PC chambers are more concentrated and imply more devastating consequences.

In conclusion, numerical modeling using the 3D model indicates that opening is ineffective in mitigating the damage of spherical chambers. Openings weaken the structure and induce local stress and damage concentration during the dynamic response of the chamber. In terms of global chamber response, the radial response of PC chambers is almost unaltered by openings, and the total plastic energy of the chamber is similar to the observed for the FC chambers. These results confirm the conclusions derived by using the SDOF analysis, which shows that ventilation is ineffective in reducing the chamber response and damage (Hernandez et al., 2019). Moreover, the 3D model shows that damage is not uniformly distributed because of stress concentrations caused by openings, which further enforces the conclusion that small/intermediate openings are not a proper solution to improve the performance of membrane blast chambers.

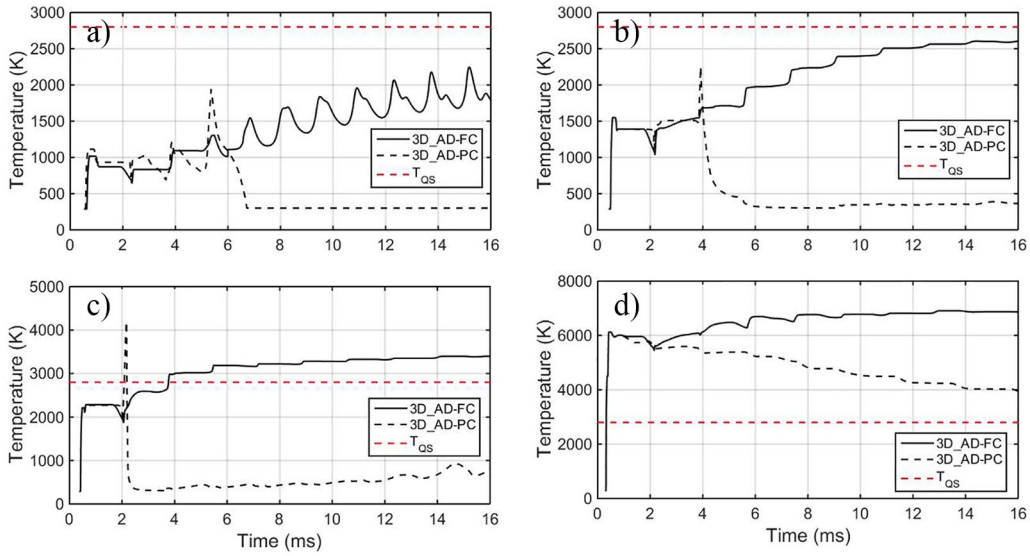

Figure 12. Temperature time histories for the fully confined (FC) and partially confined (PC) chambers: (a) $W = 7$ kg, (b) $W = 15$ kg, (c) $W = 30$ kg, and (d) $W = 120$ kg.

Temperature effects

Ventilation reliefs the internal temperature, which is another essential aspect that needs to be taken into account for the design of blast chambers. The enclosed gases increase the internal temperature and pressure because the HE chemical energy (released during the detonation and the afterburning) is transferred to gases increasing their internal and kinetic energy. The kinetic energy refers to SWs, and the internal energy is associated with the gas pressure component. At a later stage, the confined gas inside the FC chambers reaches a constant temperature and pressure associated with the QS state. In contrast, the internal temperature is rapidly reduced throughout openings, which allows the faster release of gases, and the temperature is rapidly reduced until it reaches the outside temperature. Therefore, the QS temperature is avoided if ventilation is provided, but a high flash internal temperature is observed. After the dynamic response of the chamber, a significant final temperature is observed for the FC chambers associated with the QS state. For example, the chemical equilibrium predicts that the final temperature of the gas mixture is approximately equal to $T_{QS} = 2800$ K when chambers are deficient in oxygen, that is, $W/V_{\text{vessel}} > 0.387$ kg-TNT/m^3 (Edri et al., 2013). This temperature is so high that ventilation seems to be mandatory, taking into account that the forging temperature for carbon steels is approximately 1500 K.

Figure 12 shows the temperature time-history obtained from the 3D model associated with the FC and PC chambers. It can be observed that openings allow the faster reduction of temperature (in the scale of milliseconds). The FC cases show significant QS temperatures (i.e. 1900, 2600, 3500, and 6900 K for $W = 7$, 15, 30, and 120 kg, respectively). All the studied cases refer to deficiency in oxygen chambers (i.e. $W/V_{\text{vessel}} > 0.387$ kg-TNT/m^3, Table 1) and should show a final QS temperature of 2800 K in agreement with the chemical equilibrium (Edri et al., 2013). Nevertheless, it can be observed that the QS temperature that is calculated from the 3D model disagrees with those from the chemical equilibrium approach because gases are modeled by independent EOS and are not described such as a unique gas that should be modeled by a variable gamma ideal gas EOS (Edri et al., 2013; Hernandez et al., 2016).

Ventilation reduces the exposition time that chambers are subjected to high temperatures, generating a flash temperature and avoiding that the final QS temperature is reached. This aspect should be considered in the design of explosion chambers and may be mandatory to provide ventilation when the blast load density is relatively high (e.g. $W/V_{\text{vessel}} > 0.03\,\text{kg-TNT/m}^3$ related to $T_{QS} = 650\,\text{K}$ (Edri et al., 2013)). This second design aspect needs to be further studied, considering proper material models that account for temperature effects and by using approaches that allow predicting the dynamics of the internal temperature that AUTODYN is unable to model reliably.

Spherical chambers subjected to eccentric TNT detonations

When a monobloc spherical chamber is subjected to a concentric spherical HE detonation, the blast overpressure can be described by a uniform blast loading acting on the chamber walls. Therefore, the chamber response is only described by the RBM because the modal force is null for another mode in agreement with the mode orthogonality law. When the chamber or the blast loading does not satisfy a perfect spherical symmetry, other membrane and composite modes will contribute to the chamber response. Previous studies on strain growth of the spherical chamber response showed that structural perturbation such as nozzles or flanges could introduce localized deformations (Abakumov et al., 1984; Karpp et al., 1983), which is confirmed from the 3D model of PC chambers. Previous numerical model related to uniform initial impulses shows strain growth due to linear and nonlinear modal coupling response, indicating small imperfections (associated with imperfect spherical geometry) can induce the contribution of composite modes after multiple cycles of vibration (Dong et al., 2010). In the meanwhile, the 3D model showed a stable RBM response, which is attributed to the accuracy of the AUTODYN solution, and the gas pressure component avoided an unstable RBM response. Imperfections of the spherical response occur by different reasons such as heterogenic imperfections of the material, geometrical perturbations, and asymmetries of the blast loading. In particular, the blast loading can be affected by internal asymmetries of the charge, such as an incorrect shape of the charge, its incorrect position, or its incorrect detonation point. In agreement with Sostegard's assumption (McIvor, 1966), the response of spherical chambers can be affected by slight impulse imperfections. To examine the influence of unsymmetrical detonation, the spherical TNT charge is placed 150 mm from the center of the spherical chamber ($a = 1500\,\text{mm}$, $h = 9.62\,\text{mm}$, $W = 15\,\text{kg}$). This eccentricity is equivalent to 10% of the main radius. The results of the simulation show that the peak reflected pressure is increased from 19.5 to 25.1 MPa and generates nonuniform pressure profiles.

Figure 13 shows the membrane effective plastic strain of the FC (top) and the PC chambers (bottom) corresponding to concentric TNT charges (left) and eccentric TNT charges (right). It can be observed that eccentric detonations generate localized damage near and opposite to the place where the charge was located, indicating that eccentric charges induce the response of other modes besides the RBM. It can also be observed that eccentric explosions also generate significant damage around openings. Therefore, it can be concluded that opening is not necessarily a proper choice to reduce damage, although it relieves blast loads and high temperatures associated with confined detonations. Results of these simulations demonstrate that imperfections such as eccentricity TNT charge weights can generate significant localized damage and should be studied with FEA. Therefore, the correct design of explosion chambers should consider possible perturbations associated with the blast loading and geometrical imperfections because such imperfection can generate more considerable localized damage.

Conclusion

This article carried out numerical simulations on fully and PC spherical chambers subjected to internal detonations. Overall, openings modify the pressure time-history by reducing the gas pressure

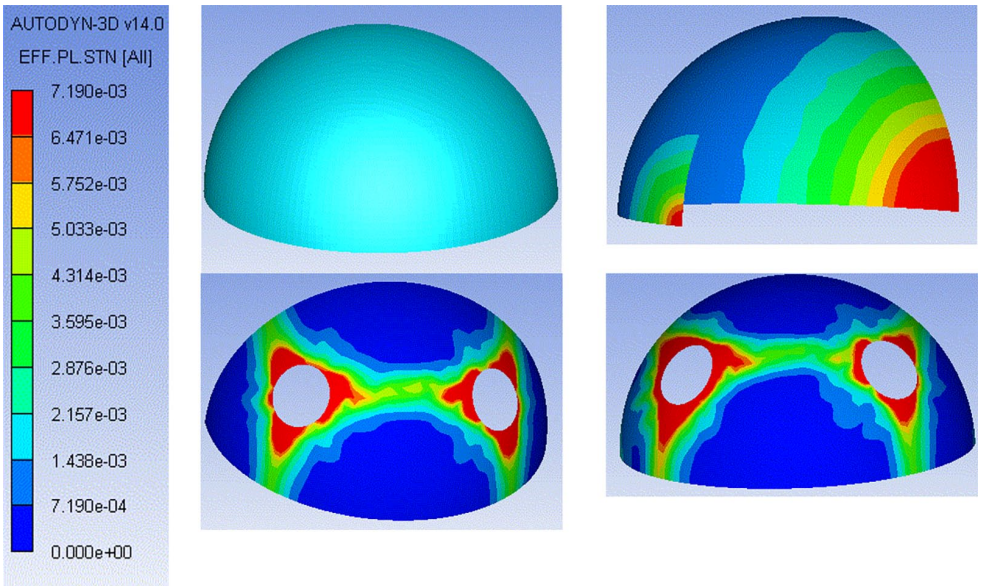

Figure 13. Effective plastic strain (ε_p) of the FC (top) and PC (bottom) chambers ($a = 1500$ mm, $h = 9.62$ mm, $W = 15$ kg) for the middle-plane (membrane) with concentric (left) and eccentric TNT charges (right).

component and also mitigate secondary re-reflected shock waves. The structural response of a spherical chamber subjected to a concentric detonation is described by the RBM and can be simplified by an SDOF system. It was observed that the natural frequencies of spherical chambers could be significantly high and comparable with the reverberation frequency that the SW impinges the chamber wall. In this context, shock waves play the leading role in the dynamic response. Despite that the pressure component can also play a significant role on the chamber response, its reduction due to small/intermediate ventilation can be ignored as the peak dynamic response is not significantly reduced due to ventilation, because the peak response is observed during the initial phase of the response (due to the effect of the initial shock waves and when the gas pressure component is not significantly mitigated). Moreover, it has been observed that the secondary re-reflected shock waves can amplify the structural response due to elastic or plastic resonance. In contrast, the presence of opening can modify the structural response generating local weaknesses that can produce local damage due to stress concentration.

The numerical results were compared and found to agree well with the authors' simplified SDOF. Through numerical simulation, it was found that small/intermediate openings are ineffective in mitigating the damage of membrane chambers during the vibratory response phase. Openings can generate stress concentrations and localized damages, which can reduce the capacity of the blast chamber to resist internal detonations. Nevertheless, ventilation allows relieving the QS temperature that is observed when FC explosions occur, which can mandate the use of ventilation when the blast density is high (e.g. $W/V_{vessel} > 0.03$ kg-TNT/m^3).

Coupled and uncoupled 3D models demonstrate that the RBM governs the responses of FC spherical chambers subjected to concentric HE detonation. So, the equivalent SDOF analysis is accurate to model the chamber response when perfect spherical symmetry is analyzed. Strong shock waves could force the chamber to respond plastically and resonate with the re-reflected shock waves, which can increase the chamber response significantly.

The current simplified approach that is used to model re-reflected shock waves might lead to significant underestimation/overestimation of chamber responses owing to the inaccurate assumption of the propagation velocity associated with secondary shock waves and its attenuation. Geometrical chamber and blast singularities should be considered for the design of blast chambers because they can drastically modify the chamber performance generating localized damage and variations of the chamber response. Therefore, 3D FEA should be used to model the blast loading accurately, and chamber imperfections that simplified approaches are unable to model.

Ventilation seems to be ineffective in mitigating the damage of membrane vessels, owing to the fact that the reduction of the gas pressure component is not fast enough to reduce significantly the maximum response and damage of structures, whose response is described by high frequencies. Meanwhile, membrane chambers are susceptible to resonance due to re-reflected shock waves. Despite the fact that ventilation mitigates re-reflected shock waves, its effect seems to be smaller than the negative effect generated by the local damages induced by openings. In contrast, structures that respond slowly, such as cubical chambers, display an initial bending response associated with lower frequencies; therefore, they can be significantly affected by the reduction of the gas pressure component and ventilation. Therefore, ventilation could be useful if chambers are governed by initial low frequencies, owing to the fact that the peak response is related to the impulse observed until the peak response is observed.

Acknowledgements

The authors acknowledge partial financial supports from the Australian Research Council (ARC) carrying out this research. The first author acknowledges the Chilean government for providing scholarship to study a PhD program in Australia. The authors also acknowledge the support from China National 973 project (2015CB058003) for carrying out field blasting tests for this project.

Declaration of conflicting interests

The author(s) declared no potential conflicts of interest with respect to the research, authorship, and/or publication of this article.

Funding

The author(s) received no financial support for the research, authorship, and/or publication of this article.

ORCID iD

Francisco Hernandez https://orcid.org/0000-0002-3723-5394

References

Abakumov AI, Egunov VV, Ivanov AG, et al. (1984) Calculation and experiments on the deformation of explosion-chamber shells. *Journal of Applied Mechanics and Technical Physics* 25: 455–458.

Anderson CE, Baker WE, Wauters DK, et al. (1983) Quasi-static pressure, duration, and impulse for explosions (e.g. HE) in structures. *International Journal of Mechanical Sciences* 25: 455–464.

Baker WE and Allen FJ (1958) The response of elastic spherical shells to spherically symmetric internal blast loading. In: *Proceedings of the third U.S. national congress of applied mechanics*, March 1958, pp. 79–87. New York: ASME.

Buzukov AA (1980) Forces produced by an explosion in an air-filled explosion chamber. *Combustion, Explosion and Shock Waves* 16: 555–559.

Chopra A (1995) *Dynamic of Structures*. Upper Saddle River, NJ: Prentice Hall.

Dong Q, Hu BY, Chen SY, et al. (2012) Engineering Design of a Multiple-Use Spherical Explosion Containment Vessel Subjected to Internal Blast Loading From 25 kg TNT High Explosive. *Journal of Pressure Vessel Technology* 134: 021205.

Dong Q, Li QM and Zheng JY (2010) Further study on strain growth in spherical containment vessels subjected to internal blast loading. *International Journal of Impact Engineering* 37: 196–206.

Dong Q, Li QM and Zheng JY (2011) Guidelines for the design of multiple-use explosion containment vessels based on the understanding of the strain growth phenomenon. *Journal of Performance of Constructed Facilities* 25: 394–400.

Edri I, Feldgun VR, Karinski YS, et al. (2012) On blast pressure analysis due to a partially confined explosion: III. Afterburning effect. *International Journal of Protective Structures* 3: 311–331.

Edri I, Feldgun VR, Karinski YS, et al. (2013) Afterburning aspects in an internal TNT explosion. *International Journal of Protective Structures* 4: 97–116.

Hernandez F (2016) *Explosive Protection of Storage Chambers Through Frangible Structural Elements*. Perth, WA, Australia: The University of Western Australia.

Hernandez F, Hao H and Abdel-Jawad M (2016) Additional afterburning energy value to simulate fully confined trinitrotoluene explosions. *International Journal of Protective Structures* 7: 232–264.

Hernandez F, Hao H and Zhang X (2019) On the effectiveness of ventilation to mitigate the damage of spherical chambers subjected to confined trinitrotoluene detonations. *Advances in Structural Engineering* 22: 486–501.

Karpp RR, Duffey TA and Neal TR (1983) Response of containment vessels to explosive blast loading. *Journal of Pressure Vessel Technology* 105: 23–27.

McIvor IK (1966) Axisymmetric response of a closed spherical shell to a nearly uniform radial impulse. *Journal of the Acoustical Society of America* 40: 1540.

Shin J, Whittaker AS, Cormie D, et al. (2014) Numerical modeling of close-in detonations of high explosives. *Engineering Structures* 81: 88–97.

Trabia MB, O'Toole BJ, Thota J, et al. (2008) Finite element modeling of a lightweight composite blast containment vessel. *Journal of Pressure Vessel Technology* 130: 011205.

UFC 3-340-02 (2008) Structures to resist the effects of accidental explosions. In: *Proceedings of the conference on structures congress*, Las Vegas, NV, 14–16 April 2011.

Zhdan SA (1981) Dynamic load acting on the wall of an explosion chamber. *Combustion, Explosion and Shock Waves* 17: 241–244.